FOUNDATIONS
ADVANCES

ISSN: 2053-2733
journals.iucr.org/a

Computer simulations of X-ray six-beam diffraction in a perfect silicon crystal. II

V. G. Kohn

Acta Cryst. (2017). A**73**, 30–38

Acta Cryst A FOUNDATIONS ADVANCES

ISSN 2053-2733

Computer simulations of X-ray six-beam diffraction in a perfect silicon crystal. II

V. G. Kohn*

National Research Centre 'Kurchatov Institute', 123182 Moscow, Russian Federation. *Correspondence e-mail: kohnvict@yandex.ru

Received 6 October 2016
Accepted 8 November 2016

Edited by L. D. Marks, Northwestern University, USA

Keywords: X-ray diffraction; silicon crystal; six-beam diffraction; section topography; computer simulations.

This paper reports computer simulations of X-ray six-beam (000, 220, 242, 044, −224, −202) diffraction in a perfect silicon crystal of large thickness where the super-transmission effect prevails, *i.e.* about 2 cm or more for an X-ray photon energy of 8 keV. Both the plane-wave angular dependence and the six-beam section topographs, which are obtained in experiments with a two-dimensional slit, are calculated. The angular dependence is computed by means of an eigenvalue problem in accordance with Ewald's theory. The section topographs are calculated by means of a fast Fourier transformation procedure from the angular to real space. It is shown that under the effect of X-ray super-transmission the quadrupole part of the photoelectric absorption as well as the Compton scattering give apparent contributions to the minimum absorption coefficient. Comparison of experimental and theoretical results by means of measuring the effective absorption coefficient is proposed. The section topographs for a thick crystal are asymmetric and polarization sensitive. These properties are explained through the angular dependence and the stationary phase method.

1. Introduction

This paper presents the results of the second part of our work, the first part being published by Kohn & Khikhlukha (2016) and referred to below as [1]. As was shown in [1], two-dimensional section topography is a suitable method for studying the six-beam (000, 220, 242, 044, −224, −202) X-ray diffraction in a perfect Si crystal. It is especially useful in experiments with synchrotron radiation (SR). Fig. 1 shows a scheme of a possible experiment.

A narrow beam from the SR source (a bending magnet or an undulator) is restricted by a two-dimensional (square) slit which is located at a long distance Z_0 (from 30 to 100 m) from the source. Such an arrangement allows one to reach a high degree of spatial coherence of radiation if the angular size of the source $A_{so} = S/Z_0$ is much less than the angular divergence of radiation due to a diffraction on the slit $A_{sl} = \lambda/D$. Here S is the source linear size (FWHM), λ is the radiation wavelength, D is the linear size of the square slit. This condition is more commonly known in the form $D < L_{tc}$, where $L_{tc} = \lambda Z_0/S$ is the length of transverse (spatial) coherence.

The dynamical theory of multiple diffraction was formulated by Ewald and Laue for monochromatic plane waves; for more details see the books by Chang (2004) and Authier (2005). This theory allows one to understand the phenomenon in terms of dispersion surface, Bloch eigenwaves, absorption coefficients. On the other hand, for a very narrow in space beam another method of calculation exists which is based on the n-beam Takagi equations (Okitsu, 2003).

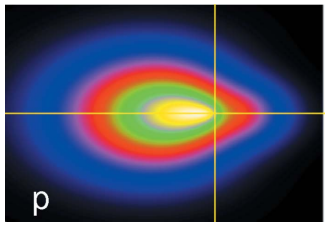

In the works of Okitsu *et al.* (2003, 2006, 2012) the *n*-beam Takagi equations were numerically solved and the results were compared with the experimental topographs. A rather good agreement was achieved for a relatively thick crystal when the size of the two-dimensional slit (pinhole) is much less than the size of the topograph. However, these computer simulations of multiple diffraction demand a supercomputer and a huge amount of computing time (more than 2 h).

In [1] we have proposed another way to perform computer simulations of section topographs for a multiple X-ray diffraction. One can calculate first the angular dependence of amplitudes of the transmitted and reflected plane waves. Then the section topograph, for example, for a transmitted wave can be calculated *via* a Fourier transformation of the amplitude using the fast Fourier transformation (FFT) procedure. This way is correct for perfect crystals, and it allows one to easily take into account the size of the two-dimensional slit and the distance between the slit and detector. The calculation time is less than 10 min for a standard laptop.

In the present work, the results of an analysis of the effect of a strong decrease in the X-ray beam absorption in a crystal due to six-beam diffraction are discussed. This effect was first formulated by Joko & Fukuhara (1967) and later investigated in more detail by Afanas'ev & Kohn (1977). It is known that, in the normal case, when there is no multiple diffraction, the dipole part of the photoelectric absorption provides the main contribution to the total absorption coefficient. We show that under conditions of six-beam diffraction the quadrupole part of the photoelectric absorption is as important as the dipole part, and there is also absorption due to Compton scattering.

We propose a way of measuring the effective absorption coefficient *via* a measurement of the total intensity of all beams that leave the crystal. This method is simple to perform because a strong collimation of the incident beam is not necessary. In this case, it is sufficient to calculate only the angular dependence of the intensity of all diffracted beams. Finally, we have calculated a section topograph of the transmitted beam for a rather thick crystal (of thickness 2 cm) which is 20 times greater than in [1].

All calculations were performed for the energy $E = 8$ keV which is close to the Cu $K\alpha$ line of the X-ray tube. It is convenient to study the phenomenon of decreasing absorption under the conditions when normal absorption is sufficiently strong that the required thickness of the crystal can be reduced.

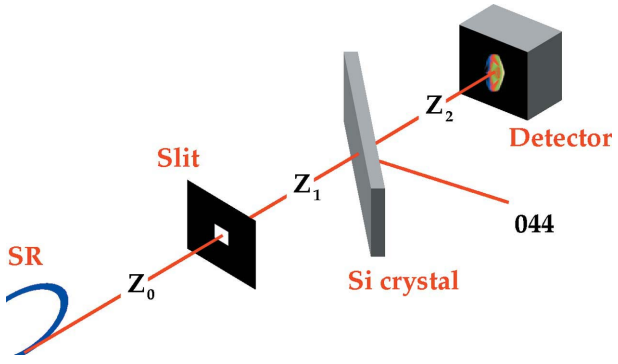

Figure 1
A scheme of a possible experiment for six-beam diffraction section topography.

2. Various channels of X-ray absorption

The geometry of six-beam diffraction is shown in Fig. 1 of [1]. Here we repeat definitions of geometrical parameters. We consider a silicon crystal in the form of a plate of thickness t with a surface normal to the unit vector $\mathbf{n}_0$ which has a direction along the (1−11) of the cubic crystal lattice. The wavevector of the incident plane wave $\mathbf{k}_0$ forms the angle θ_0 with the vector $\mathbf{n}_0$, and $\sin\theta_0 = 8^{1/2}\lambda/a$, where a is the crystal lattice parameter. Then, for six reciprocal-lattice vectors $\mathbf{h}_m$ the Bragg condition $|\mathbf{k}_m|^2 = |\mathbf{k}_0|^2$ is met, where $\mathbf{k}_m = \mathbf{k}_0 + \mathbf{h}_m$. Here, the index $m = 0, \ldots, 5$ and its values correspond to the Miller indices (000, 220, 242, 044, −224, −202).

We introduce the function $P_{Cf}^{vv'}(q, p, t, m)$ which was considered in [1] for $m = 0$ (transmitted beam). It describes the angular dependence of the amplitude of the mth diffracted plane wave at the exit surface of the crystal. This angular dependence is defined by coordinates q and p of the two-dimensional vector $\mathbf{u}$ in the plane normal to $\mathbf{k}_0$. Below, we show briefly how the function $P_{Cf}^{vv'}$ can be calculated. If the incident plane monochromatic wave has a wavevector $\mathbf{k}'_0 = \mathbf{k}_0 + \mathbf{u}$, then inside the crystal it experiences refraction and the wavevector becomes equal to $\mathbf{k}'_0 + \varepsilon\mathbf{n}_0/2$. Diffraction causes the appearance of additional plane waves with the wavevectors $\mathbf{k}'_m + \varepsilon\mathbf{n}_0/2$, where $\mathbf{k}'_m = \mathbf{k}'_0 + \mathbf{h}_m$.

The vector amplitude of the electric field of the mth diffracted plane wave has two components in the plane normal to $\mathbf{k}_m$. We enumerate these components by the index v. Sometimes we will denote the values of v as p, s. It is possible to distinguish between p as the coordinate of $\mathbf{u}$ and p as the polarization state (value of v) from the context. For each plane wave we have three unit vectors $\mathbf{e}_{mp}$, $\mathbf{e}_{ms}$ and $\mathbf{s}_m$ where $\mathbf{s}_m = \mathbf{k}_m/K$ is a unit vector along the mth beam direction, $K = 2\pi/\lambda$ is a wavenumber. It is convenient to use symmetry properties of the multi-beam pyramid, as was first proposed in the work of Joko & Fukuhara (1967). In this case, all the vectors $\mathbf{e}_{ms}$ lie in the plane of reciprocal-lattice vectors and $\mathbf{e}_{mp} = [\mathbf{e}_{ms} \times \mathbf{s}_m]$.

We denote the scalar components of the electric field vector by $\gamma_m^{-1/2}E_{mv}$, where the multiplier $\gamma_m = (\mathbf{s}_m\mathbf{n}_0)$ is introduced for convenience. Then, a standard procedure of averaging Maxwell's equation for the total electric field in the crystal over a unit cell leads to a division of one equation into a system of equations for each component E_{mv}. This system can be written in the form of the eigenvalue problem:

$$\sum_{nv'} G_{mn}^{vv'} E_{nv'} = \varepsilon E_{mv} \qquad (1)$$

for the scattering matrix G, which has the following form in the dipole approximation:

$$G_{mn}^{vv'} = -\frac{K\alpha_m}{\gamma_m}\delta_{mn}\delta_{vv'} + \frac{K\chi_{m-n}}{(\gamma_m\gamma_n)^{1/2}}(\mathbf{e}_{mv}\mathbf{e}_{nv'}). \qquad (2)$$

Here, δ_{mn} equals 1 if $m = n$, and 0 otherwise, the parameters $\alpha_m = (|\mathbf{k}'_m|^2 - |\mathbf{k}'_0|^2)/K^2$ depend on the angles $\theta = q/K$ and $\varphi = p/K$, and the diffraction parameter χ_m is the complex value that describes the amplitude of the kinematical scattering by unit volume of the crystal. The matrix G in equation (1) describes both the elastic scattering (the real part of the matrix G') and the absorption (the imaginary part of the matrix G''). In our case the matrix elements of G'' are much less than the matrix elements of G', which allows us to take them into account by means of perturbation theory.

Therefore, the eigenvalue problem (1) is solved only for the real matrix G' which speeds up calculations. As a result of solution, we obtain $2N$ real eigenvectors and $2N$ real parts of eigenvalues, where $N = 6$ is the number of beams for our case. The absorption coefficients as imaginary parts of eigenvalues are calculated later by means of the formula

$$\mu_j = \varepsilon''_j = \sum_{mv,nv'} E^{(j)}_{mv} (G'')^{vv'}_{mn} E^{(j)}_{nv'} \tag{3}$$

where the index j enumerates the eigensolutions.

We note that equation (2) is close to the accurate one only for the real part of the matrix G' when it is sufficient to consider only the dipole part of the scattering matrix. The reason is that the Thomson scattering of X-rays on the electron density of atoms gives the main contribution, and it has a purely dipole character. In this approximation

$$\chi'_m = -\frac{\lambda^2 r_0}{\pi V_0} \sum_k N_k \left[f_k(g_m) + \Delta f_{1k} \right] F_k(g_m) S_k(\mathbf{h}_m) \tag{4}$$

where $r_0 = e^2/mc^2$ is the classic electron radius, e and m are the charge and mass of an electron, c is the speed of light, V_0 is the volume of the unit cell.

A summation is carried out over the various kinds of atoms; N_k is the number of atoms of kind k inside the unit cell, $f_k(g)$ is the Fourier image of atomic electron density (atomic factor), $g_m = |\mathbf{h}_m|/4\pi = \sin\theta_B/\lambda$, θ_B is the Bragg angle for the diffraction on the reciprocal-lattice vector $\mathbf{h}_m$. We note that $f_k(0) = Z_k$ is the number of electrons in an atom. The parameter Δf_{1k} is an additional term to the atomic factor due to the photoelectric absorption. The parameter $F_k(g)$ is the thermal factor and $S_k(\mathbf{h}_m)$ is the structure factor,

$$F_k(g) = \exp(-8\pi^2 g^2 \langle u_k^2 \rangle),\ S_k(\mathbf{h}_m) = n_k^{-1} \sum_{i=1}^{n_k} \exp(-i\mathbf{h}_m \mathbf{r}_{ik}), \tag{5}$$

where $\langle u_k^2 \rangle$ is the mean square thermal displacement of an atom, $\mathbf{r}_{ik}$ is the position of the ith atom of the kth kind, n_k is the number of such positions. We note that $F_k^2(g)$ equals the Debye–Waller factor, and in our case $S_k(\mathbf{h}_m) = 1$ for all reflections.

The imaginary part G'' is determined only by the processes of photoelectric absorption and Compton scattering. The photoelectric interaction of radiation with an atom occurs on the inner atomic shells which have a small but finite size. Therefore, both the intensity of radiation and the first spatial derivative of intensity are important. They correspond to the dipole and quadrupole terms of multipole expansion. As a result we have

$$(G''_{\mathrm{PEA}})^{vv'}_{mn} = \frac{K(\chi''_{m-n})_{\mathrm{PEA}}}{(\gamma_m \gamma_n)^{1/2}} \{(1-Q)(\mathbf{e}_{mv}\mathbf{e}_{nv'}) + Q[(\mathbf{e}_{mv}\mathbf{e}_{nv'})(\mathbf{s}_m\mathbf{s}_n) + (\mathbf{e}_{mv}\mathbf{s}_n)(\mathbf{e}_{nv'}\mathbf{s}_m)]\} \tag{6}$$

where PEA stands for photoelectric absorption. Here $(\chi''_m)_{\mathrm{PEA}}$ has to be calculated from the experimental value of the photoelectric absorption coefficient,

$$(\chi''_m)_{\mathrm{PEA}} = \frac{\lambda^2 r_0}{\pi V_0} \sum_k N_k f_{2k} F_k(g_m) S_k(\mathbf{h}_m), \tag{7}$$

where f_{2k} is an additional imaginary term to the atomic factor due to a photo effect, which can be obtained from the tables (we use the DABAX table from http://ftp.esrf.eu/pub/scisoft/xop2.3/DabaxFiles/) together with the Δf_{1k}. They are independent of the index of reflection because it has very weak angular dependence. The parameter $Q = \sigma_Q/(\sigma_D + \sigma_Q)$, where $\sigma_{D,Q}$ are cross sections of the dipole and quadrupole contributions to the photoelectric absorption. The values of Q were calculated by Hildebrandt *et al.* (1975). In our case $Q = 0.019$.

Compton scattering occurs on all electrons of an atom but this interaction is not local. In the normal case the X-ray absorption due to Compton scattering is very weak and can be neglected. However, under conditions of the Borrmann effect, when the photoelectric absorption decreases, this channel becomes relatively more important and needs to be accounted for. This fact was first noted by Giardina & Merlini (1973) for the two-beam case. The suitable formulae were derived by Sano *et al.* (1969). Taking into account the results of this work, for the case of a crystal having atoms of the same kind ($k = 1$), we can write

$$(G''_{\mathrm{CS}})^{vv'}_{mn} = \frac{8\pi r_0^2 N_1}{3V_0} F_1(g_{m-n}) \left[f_1(g_{m-n})(\mathbf{e}_{mv}\mathbf{e}_{nv'}) - \Delta^{vv'}_{mn} \right] \tag{8}$$

where

$$\Delta^{vv'}_{mn} = \frac{3}{8\pi} \int \mathrm{d}\mathbf{s} [(\mathbf{e}_{mv}\mathbf{e}_{nv'}) - (\mathbf{e}_{mv}\mathbf{s})(\mathbf{e}_{nv'}\mathbf{s})] \times \sum_{\alpha\beta} f_1^{\alpha\beta}(\mathbf{s} - \mathbf{s}_m) f_1^{\beta\alpha}(\mathbf{s}_n - \mathbf{s}). \tag{9}$$

Here the functions $f_1^{\alpha\beta}(\mathbf{s})$ mean the matrix elements between the atomic electron states α and β from the quantity $\sum_i \exp(iK\mathbf{s}\mathbf{r}_i)$ where $\mathbf{r}_i$ is a vector of position of the ith electron, and the summation is carried out over all electrons. We note that $f_1(g_{m-n}) = \sum_\alpha f_1^{\alpha\alpha}(\mathbf{s}_m - \mathbf{s}_n)$.

We do not know the tables for the functions $f_1^{\alpha\beta}(\mathbf{s})$ similar to the tables for $f_1(g)$, and there is a problem in calculating the matrix $\Delta^{vv'}_{mn}$. Fortunately, we can conclude that multiple diffraction will lead to a decrease in the term containing $\Delta^{vv'}_{mn}$ similarly to the dipole part of the photoelectric absorption because it depends weakly on the reciprocal-lattice vectors of reflections. Therefore, we can neglect this term and consider only the first term in the square brackets of equation

Table 1
The input data for computer simulations.

hkl	θ_B (°)	$K\chi'_m$ (0.1 μm^{-1})	$K\chi''_m$ (0.01 μm^{-1})
000	0	−6.236827	1.433822
220	23.80108	−3.811071	1.389435
242	44.34609	−2.781228	1.304741
044	53.81598	−2.439140	1.264350

(8). In this approximation we have a relation $(G''_{CS})^{\nu\nu'}_{mn} = -(4\pi r_0/3\lambda)(G')^{\nu\nu'}_{mn}$ where the matrix G' is taken at the point $\theta = \varphi = 0$.

Finally, taking into account boundary conditions, as was shown in [1], we can write

$$P^{\nu'\nu}_{Cf}(q,p,t,m) = \left(\frac{\gamma_0}{\gamma_m}\right)^{1/2} \sum_j E^{(j)}_{m\nu'} E^{(j)}_{0\nu} \exp(i\varepsilon_j t/2) \qquad (10)$$

where j is an index of the eigensolution and ε_j is a complex value so that the absorption coefficient $\mu_j = \varepsilon''_j$. We note that the quantity $(E^{(j)}_{0\nu})^2$ has a sense of excitation degree for the jth eigensolution (Bloch wave) and for the ν-polarized incident wave.

We have performed a numerical solution of the eigenvalue problem of equation (1) at the central point $\theta = \varphi = 0$, taking into account various channels of absorption, *i.e.* dipole (D), quadrupole (Q) and Compton (C) channels, for the photon energy E = 8 keV. The input data for a calculation are shown in Table 1. The parameters $K\chi''_m$ in Table 1 are shown for the sum of all channels D + Q + C; the calculations were also performed for three cases – with the D channel only, D + Q channels and all three channels. The results are shown in Table 2.

As shown by Afanas'ev & Kohn (1977), at this point the eigenvalue problem has an analytical solution which can be derived from the symmetry properties. There are four twice-degenerated solutions which are excited for both polarizations p and s. They are denoted as 1ps +, 1ps−, 2ps +, 2ps−. There are four non-degenerated solutions which are excited only for one polarization, and they are denoted 3p, 3s, 6p, 6s.

Since the degenerated solutions have the same eigenvalue, the only sum of their excitation degree has a physical meaning. Therefore, in Table 2 we show only eight various eigen-solutions and their excitation degrees. The line corresponding to number 9 shows the values for a normal case, *i.e.* without diffraction. In this case, an absorption coefficient is equal to a mean value and an excitation degree equals the sum of all the above-mentioned values.

The solution 3p with a minimum absorption coefficient is excited only for p polarization. There are three solutions with very small absorption coefficients. One can see that the p polarization is more excited for all three solutions. The table clearly shows that we cannot neglect quadrupole and Compton channels of absorption in estimating the minimum absorption coefficient because all three channels give comparable contributions.

Table 2
The absorption coefficients in cm^{-1} for dipole (D), quadrupole (Q), Compton (C) channels of absorption, and the excitation degrees (ED) (p and s polarizations) for various eigensolutions at the central point $\theta = \varphi = 0$.

n	Type	D	D + Q	D + Q + C	ED p	ED s
1	1ps−	928.88	913.09	915.14	0.105	0.228
2	6p	907.30	907.87	909.92	0.167	0.000
3	6s	43.05	42.53	43.15	0.000	0.167
4	2ps−	29.09	39.99	40.49	0.101	0.232
5	1ps+	23.18	27.53	27.97	0.228	0.105
6	3s	0.68	1.20	1.47	0.000	0.167
7	2ps+	0.39	0.56	0.80	0.232	0.101
8	3p	0.25	0.43	0.67	0.167	0.000
9	Norm	242.86	242.86	243.66	1.000	1.000

3. Effective absorption coefficient

There is a problem in measuring the plane-wave minimum absorption coefficient. For this experiment one needs to collimate strongly the incident beam because the angular dependence of small absorption coefficients is very strong. Instead, one can use the experimental scheme shown in Fig. 1 with the two-dimensional slit. In this scheme it is necessary to measure the integral intensity of all beams leaving the crystal through the exit surface. In other words, we need to measure the z component of the Poynting vector $S_{zv}(t)$ where v is an index of incident wave polarization.

In reality, one can register section topography pictures for all beams and calculate the intensity in all pixels. There is another way, namely, to use a detector with a big window placed just behind the crystal. Then, all beams will go to the same detector. To calculate this value we have the formula

$$S_{zv}(t) = \sum_{m\nu'} \gamma_m \int \mathrm{d}x\,\mathrm{d}y \left|\psi^{\nu'\nu}_m(x,y)\right|^2. \qquad (11)$$

On the other hand, as was shown in [1], the section topograph of the mth beam is described by the following formula:

$$I_{m\nu}(x,y) = \sum_{\nu'} \left|\psi^{\nu'\nu}_m(x,y)\right|^2 \qquad (12)$$

where

$$\psi^{\nu'\nu}_m(x,y) = \int \frac{\mathrm{d}q\mathrm{d}p}{(2\pi)^2} \exp(iqx + ipy) \times P^{\nu'\nu}_{Cf}(q,p,t,m) P_{2f}(q,p,z_t) T_f(q,p). \qquad (13)$$

Here $z_t = Z_1 + Z_2$, and the distances Z_1 and Z_2 are shown in Fig. 1,

$$P_{2f}(q,p,z) = \exp\left[-i\frac{\lambda z}{4\pi}(q^2+p^2)\right], \qquad (14)$$

$$T_f(q,p) = 4x_0 y_0 \,\mathrm{sinc}\,(qx_0)\,\mathrm{sinc}\,(py_0), \qquad (15)$$

$$\mathrm{sinc}\,(x) = \frac{\sin(x)}{x}. \qquad (16)$$

The parameters x_0 and y_0 represent half the size of the two-dimensional slit horizontally and vertically. For a square slit $y_0 = x_0$.

Table 3
The effective absorption coefficient for $E = 8$ keV, $t - t_0 = 0.2$ cm.

t (cm)	μ^p_{e1} (cm^{-1})	μ^s_{e1} (cm^{-1})	μ^p_{e2} (cm^{-1})	μ^p_{e2} (cm^{-1})
2	2.08	2.74	1.15	1.39
3	1.74	2.24	1.02	1.18
5	1.42	1.77	0.89	0.97
8	1.21	1.45	0.81	0.85

It is easy to verify that

$$\int \mathrm{d}x\,\mathrm{d}y \left|\psi_m^{\nu'\nu}(x,y)\right|^2 = \int \frac{\mathrm{d}q\mathrm{d}p}{(2\pi)^2} \left|P_{Cf}^{\nu'\nu}(q,p,t,m)\right|^2 \left|T_f(q,p)\right|^2. \tag{17}$$

Then

$$\gamma_m \left|P_{Cf}^{\nu'\nu}(q,p,t,m)\right|^2 = \gamma_0 \sum_j \left(E_{m\nu'}^{(j)} E_{0\nu}^{(j)}\right)^2 \exp(-\mu_j t) + 2\gamma_0 \sum_{j<j'} E_{m\nu'}^{(j)} E_{0\nu}^{(j)} E_{m\nu'}^{(j')} E_{0\nu}^{(j')} \times \cos[(\varepsilon'_j - \varepsilon'_{j'})t/2] \exp[-(\mu_j + \mu_{j'})t/2]. \tag{18}$$

The second term in equation (18) contains an oscillating multiplier with a very small period of oscillation for a large crystal thickness t. Since we are interested in only integral value (17), this term can be neglected. We can also use the relation $\sum_{m\nu'} (E_{m\nu'}^{(j)})^2 = 1$ which follows from the property of eigensolutions.

Finally, we introduce the effective absorption coefficient (EAC) of the first kind by means of the formula

$$\exp(-\mu_{e1}^{(\nu)} t) = \frac{S_{z\nu}(t)}{S_{z\nu}(0)} = A^{-1} \int \frac{\mathrm{d}q\mathrm{d}p}{(2\pi)^2} \left|T_f\right|^2 C_\nu(t) \tag{19}$$

where $A = 4x_0y_0$ is a slit area,

$$C_\nu(q,p,t) = \sum_j \left(E_{0\nu}^{(j)}\right)^2 \exp(-\mu_j t). \tag{20}$$

The integral in equation (19) is easy to calculate because the integrand depends weakly on q and p, and very many points are not necessary. However, this definition is not complete. Indeed, we can fix the slit at the position normal to the beam, but the crystal can be rotated on arbitrary angles. This will give various values. Therefore, we propose selecting such angular positions of the crystal for which $\mu_{e1}^{(\nu)}$ reaches the minimum value.

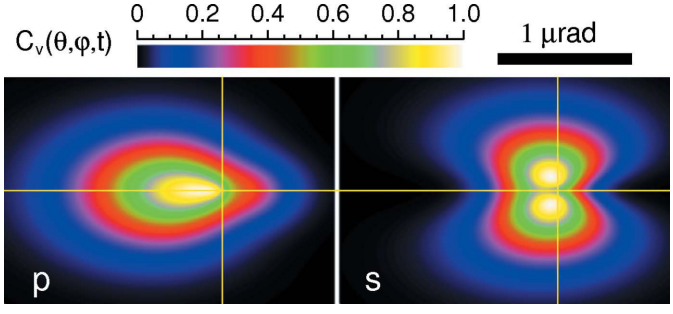

Figure 2
The functions $C_\nu(\theta, \varphi, t)$ for $\nu = p$ (left) and $\nu = s$ (right) for $t = 8$ cm. The θ (horizontal) and φ (vertical) axes have the same units which are shown above the colour maps. The contrast is shown from zero to maximum values which are equal to 1.55×10^{-3} for p and 2.41×10^{-4} for s polarizations.

Since the function $C_\nu(t)$ is symmetrical over the p coordinate, this position is easily found along the p axis. In this case, the points of maximum of $|T_f|^2$ and $C_\nu(t)$ coincide. For the q axis, the situation is more complex because the function $C_\nu(t)$ is not symmetrical. Therefore, it is necessary to make a calculation for various values of an angular shift of the crystal relative to the slit. We note that the optimum position of the crystal becomes different for different polarization.

Although the integral in equation (19) is calculated in the infinite limits, the areas where the functions $|T_f|^2$ and $C_\nu(t)$ are not zero have finite sizes. It is convenient to calculate the angular dependence of each function within its area. Then, the area of integration is an intersection of two areas. This area can be different for different values of the crystal angular shift. For small crystal thicknesses the area of $|T_f|^2$ is less than that of the crystal. For large thicknesses the situation is the opposite.

We can introduce the EAC of the second kind by means of the formula

$$\exp[-\mu_{e2}^{(\nu)}(t - t_0)] = \frac{S_{z\nu}(t)}{S_{z\nu}(t_0)}. \tag{21}$$

In this case one needs to have two crystals of different thicknesses. It is more difficult to perform, but can give a smaller value of the EAC, especially for thick crystals. Indeed, the crystal of thickness t_0 now plays the role of collimator. It creates the beams of small angular divergence, and we can observe a transmission of all beams of such radiation through the crystal of thickness $(t - t_0)$. In this case, slit size is less important than in the first case.

We have performed calculations of the EACs of both kinds for various crystal thicknesses and the square two-dimensional slit with a linear size 40 μm. The case D + Q + C was considered. The results are shown in Table 3. The difference $t - t_0 = 0.2$ cm for all values of t. In accordance with the data of Table 3, EACs of both kinds for p polarization are less than EACs for s polarization. The values of EACs of the second kind are less than those of the first kind but the difference becomes smaller for large thicknesses. The difference between the two polarizations also becomes smaller for large thicknesses.

It is of interest that the values of the EAC of the second kind for $t = 8$ cm are close to the minimum values shown in Table 2. However, even for $t = 2$ cm the value of the EAC is rather small and only two eigensolutions exist for both polarizations. But it is sufficient for observing the *Pendellösung* fringes in the section topograph as will be shown below. As is known, in the two-beam case the *Pendellösung* fringes are absent under the conditions of the Borrmann effect.

On the other hand, the value of the relative transmission intensity (RTI) in this case is rather small, namely, $\exp(-\mu_{e1}^{(p)}t) = 6.25 \times 10^{-5}$ for $t = 8$ cm. There are several reasons for this intensity decrease. First, only part of the incident radiation undergoes weak absorption. Secondly, this effect is realized only within a narrow angular area near the central point while the angular area of incident radiation is much larger. It is formed by the two-dimensional slit. Of course, for a larger two-dimensional slit the relative intensity will have a larger value. However, we cannot increase the size of the two-dimensional slit infinitely because the angular divergence of the SR source limits the collimation.

It is of interest to discuss the angular dependence of the RTI for plane waves, *i.e.* without a slit influence, and for the two polarizations separately. These values are described by equation (20) if one replaces the coordinates q and p by the angles $\theta = q/K$ and $\varphi = p/K$. Fig. 2 shows this angular dependence as colour maps with a linear scale of intensity variations. The correspondence between colours and function values is shown above the maps where the value 1.0 is shown instead of the real maximum value which is different for the different polarizations. The maximum value for the p polarization is five times greater than that for the s polarization (see the figure caption).

The structure of the angular dependence is different too. The reason for this difference is the fact that for the p polarization the incident 000 wave interacts strongly with 220 and −202 reflected waves while other reflected waves, *i.e.* 242, 044 and −224, interact weakly. For the s polarization the situation is the opposite. Therefore, the region of high intensity for the p polarization is oriented between the lines of the Bragg condition for 220 and −202 reflections with a strong horizontal asymmetry, while the same region for the s polarization is oriented along the 044 line and is more symmetric.

Fig. 3 shows the angular dependence of intensity for each beam separately and for the p polarization. Fig. 4 shows the same for the s polarization. The functions shown in the figures are determined by the formula

$$C_{mv}(\theta, \varphi, t) = \sum_{j,v'} \left(E_{mv'}^{(j)} E_{0v}^{(j)} \right)^2 \exp(-\mu_j t). \qquad (22)$$

All six maps are shown on the same scale with a maximum value 5.81×10^{-4} for the p polarization which corresponds to the 000 beam, and 5.36×10^{-5} for the s polarization which corresponds to the 242 beam. These figures illustrate clearly the role of various beams for different polarizations. We can conclude that the p polarization and the 000 beam are preferred for a collimation of radiation by means of the effect of super-transmission of X-ray radiation under the conditions of six-beam diffraction. The two-dimensional angular divergence of the beam of less than 1 µrad can be achieved.

4. Section topography of a thick crystal

As was shown in [1], the section topograph of the mth beam for a perfect crystal can be calculated by means of formulae (12) and (13) *via* the Fourier image of the product of three functions. For a thick crystal the angular area of integration is rather small. Therefore, the Fourier image of the Fresnel propagator (14) for a mean distance z_t and the Fourier image of the two-dimensional slit (15) are slow functions which influence weakly the section topograph. The structure of the topograph depends mainly on the crystal diffracting properties.

Since several eigensolutions have a small absorption coefficient there is interference between them, resulting in strong oscillations of the function $P_{Cf}^{v'v}(q, p, t, m)$ in some angular regions. This is why the integral should be calculated by an FFT procedure on the set of points with a very small step. On the other hand, one needs many points to cover the area

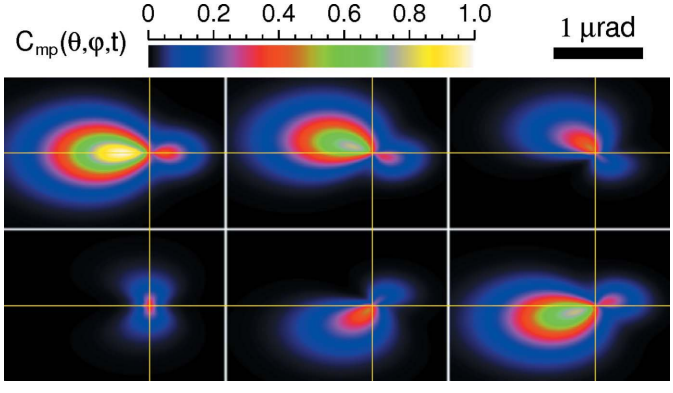

Figure 3
The functions $C_{mp}(\theta, \varphi, t)$ for various values of the reflected beam index m, *i.e.* 000, 220, 242, 044, −224, −202, and for p polarization, $t = 8$ cm. The order is from left to right and from top to bottom. The θ (horizontal) and φ (vertical) axes have the same units which are shown above the colour maps. The axes are shown by yellow lines. The contrast is shown from zero to the value 5.81×10^{-4} for all beams which is the maximum for the 000 beam.

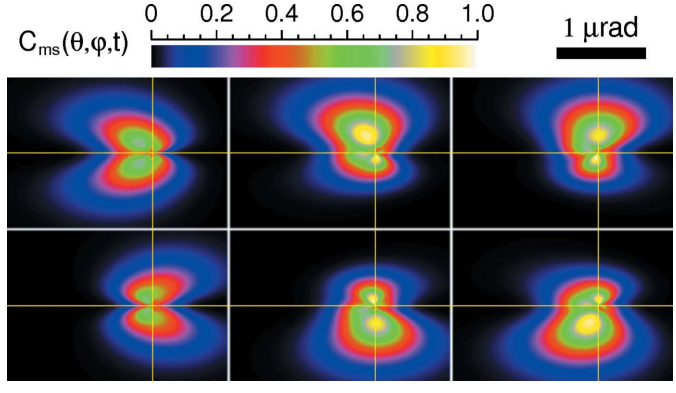

Figure 4
The functions $C_{ms}(\theta, \varphi, t)$ for various values of the reflected beam index m, *i.e.* 000, 220, 242, 044, −224, −202, and for s polarization, $t = 8$ cm. The order is from left to right and from top to bottom. The θ (horizontal) and φ (vertical) axes have the same units which are shown above the colour maps. The axes are shown by yellow lines. The contrast is shown from zero to the value 5.36×10^{-5} for all beams which is the maximum for the 242 beam.

where the function modulus has significant values. As was shown above, the transmitted beam is more interesting.

Fig. 5 shows the section topographs of the transmitted beam for the crystal thickness $t = 2$ cm which is 20 times greater than for the crystals shown in [1]. The calculation was performed for $z_t = 100$ cm, for the square slit with a linear size 40 µm and on the set of 8192 × 8192 points with the same angular step 0.0015 µrad for both directions. The array of complex numbers on this set of points demands 1 GB of computer memory. To simplify the calculation we use the properties of the functions $P_{Cf}^{\nu'y}(\theta, \varphi)$ and an FFT procedure.

First, the functions $P_{Cf}^{\nu'y}(\theta, \varphi)$ are symmetrical and decrease faster on the φ axis. Therefore, they are calculated only on the set of 8192 × 2048 points, which results in a 4× decrease in the computing time. The region $0 < \varphi < \varphi_{max}/2$ was used. The FFT procedure $\theta \rightarrow x$ was also calculated in the 2048 points for the same φ values. The functions of (x, φ) arguments were saved only in the interval $-x_{max}/2 < x < 0$, *i.e.* for 2048 points again because the functions are close to zero for other points. The FFT procedure $\varphi \rightarrow y$ was calculated in the same x interval but for 8192 points on the φ axis. For this, the functions were symmetrically enhanced on the interval $-\varphi_{max}/2 < \varphi < \varphi_{max}/2$ and other points were filled by zero values. The results were saved in the interval $-y_{max}/2 < y < y_{max}/2$ on a set of 4096 points. The pictures in Fig. 5 were obtained from arrays of 2048 × 4096 points.

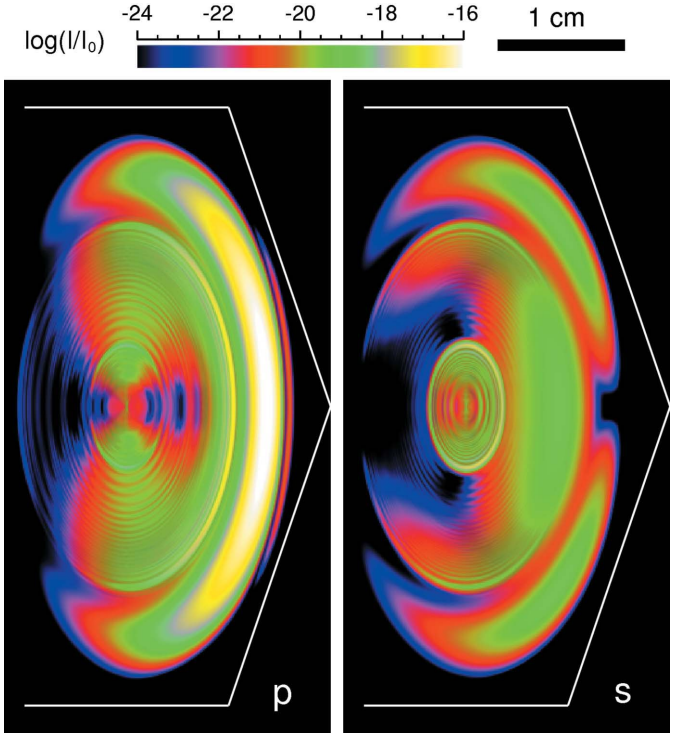

Figure 5
The section topographs of the transmitted beam for $t = 2$ cm, $z_t = 100$ cm for p (left) and s (right) polarizations. The logarithm of relative intensity is shown. The white contour shows the boundary of the multi-beam hexagon which has sizes 3.23 cm horizontally and 4.73 cm vertically. Compression of the horizontal size is due to a projection of the hexagon from the exit crystal surface to the plane normal to the transmitted beam.

The procedure described above allows us to decrease both the computing time and the computer memory. The computing time is determined mainly by the calculation of the functions $P_{Cf}^{\nu'y}(\theta, \varphi)$. The use of an FFT procedure significantly speeds up calculation of the Fourier transformation. However, one has to choose carefully the steps and number of points because they cannot be arbitrary. Sometimes the region of integration must be much larger than the region of the apparent values of the function. Such a procedure is called oversampling (Miao *et al.*, 2002).

It is known from n-beam Takagi equations that for relatively small values of both the distance z_t and the slit size, the section topography area is limited by a six-beam hexagon. In our case it has sizes $X_t = 2t \sin\theta_0 = 3.23$ cm horizontally (along the 044 reciprocal-lattice vector) and $Y_t = 2t \tan\theta_0 \sin 60^\circ = 4.73$ cm vertically, where $\theta_0 = 53.8^\circ$ (see Fig. 1 in [1]). The right-hand side of this hexagon is shown in Fig. 5. A ray along the incident beam corresponds to the extreme right point of the hexagon. This point is also the central point of the calculated area. One can see that a strong asymmetry of intensity distribution still takes place even for a thick crystal. First, for the p polarization the region of high intensity has the form of an arc at the right side of hexagon. It is of interest that this arc was observed by Umeno (1970) in the first experiment of six-beam section topography made with very low resolution.

The section topographs contain three elliptical rings for both polarizations. The outer rings are asymmetrical and do not contain interference fringes. This means that they are formed by only one eigensolution. The middle rings contain fringes and they are asymmetrical, but the asymmetry is weaker than for the outer rings. The inner ellipses have fringes and they are close to being symmetric. They are located at the centre of the hexagon. This property is similar to the two-beam case.

It is evident that just the inner ellipses are formed by the central region of angular dependence near the point (0,0) where the absorption coefficients reach minimum values. With increasing crystal thickness their visibility will increase. As was shown by Kohn & Toneyan (1986), the stationary phase method allows one to make a correspondence between the intensity of section topograph points and characteristics of plane-wave multiple diffraction such as the shape of the dispersion surface (DS), the amplitude of reflection and absorption coefficient. This correspondence is simpler when many branches of the DS (*i.e.* eigensolutions) are absorbed and do not work.

For example, the central part of the DS is symmetrical and just forms the central part of the section topograph. The left-hand part of the angular dependence forms the right-hand part of the section topograph because for this region the Poynting vector is directed close to the direction of the transmitted beam. Such a property of the DS is also known in the two-beam case. The interference fringes are not pronounced due to the fact that one of the rays has a small amplitude as a result of absorption. However, one can observe that they have variable period. It is evident that the source of

interference is the existence of several eigensolutions or branches of the DS. Nevertheless, a correspondence between a source and a result is very complicated, and additional study of the problem is necessary.

5. Discussion and conclusion

The phenomenon of X-ray six-beam diffraction in a perfect crystal and the effect of super-transmissivity is of interest mainly for the case of a plane incident wave. However, it is a very difficult task to prepare the plane wave with a high accuracy because of the very strong angular dependence of interaction between the X-ray radiation and the crystal lattice. On the other hand, six-beam section topography for a thick crystal is rather different from the two-beam case.

In the two-beam case one uses mainly the reflected beam section topographs due to their symmetry and the large period of fringes in the central part of the topograph. The interference exists only for thin crystals. For thick crystals the interference is absent, and both the incident and the reflected beams show the peak of intensity in the central part of the one-dimensional picture.

The six-beam section topographs are asymmetrical for all beams, and only the transmitted beam interacts strongly with all diffracted beams. The interference fringes exist even for a very thick crystal and have a rather complicated structure. The reason for this property is the existence of several eigensolutions with a small absorption coefficient. Below, to simplify the notation, we will use the symbol ε only for a real part, *i.e.* ε'. The imaginary part will be denoted as μ.

It is known that the functions $\varepsilon_j(\theta, \varphi)$ for various eigensolutions can be considered as various branches of the DS. The asymmetry of section topographs is a consequence of asymmetry of angular dependence of eigenvectors, particularly the excitation degrees $(E_{0v}^{(j)})^2$. For a large crystal thickness $t > 2$ cm, only three eigensolutions with indices 6, 7, 8 in Table 2 give an apparent contribution.

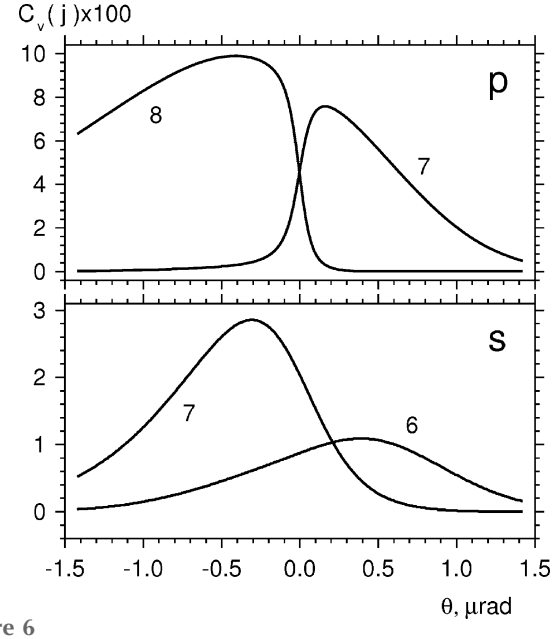

Figure 6
The curves of θ dependence of contribution of various eigensolutions to the integral transmission intensity for the crystal of thickness t = 2 cm.

Fig. 6 shows two nonzero terms,

$$C_v(j) = (E_{0v}^{(j)})^2 \exp(-\mu_j t), \tag{23}$$

in the sum of equation (20) as a function of angle θ at the line $\varphi = 0$. As follows from the calculations, the solution of index 7 stays degenerated, the non-degenerated solution of index 6 is absent for p polarization whereas the solution of index 8 is absent for s polarization. Therefore, for both polarizations only two different solutions exist.

The functions $\mu_j(\theta)$ are symmetrical and the absorption leads to a decrease in the value of the quantity (23) at large distances from the central point $\theta = 0$. However, two functions $C_v(j)$ for both polarizations have a point of maximum at opposite sides of the axis θ. The functions for p polarization have larger values and a stronger derivative at the central point.

Fig. 6 shows that the curve of each eigensolution has strong asymmetry, but different curves can compensate each other because their asymmetry is opposite. However, since the maximum values are different the compensation is not complete. On the other hand, it is easy to understand that the interference is possible only within the small region near the central point where both solutions exist simultaneously.

The fact of a strong derivative of eigenvectors at the central point follows from the existence of branches of the DS with a small distance between them. It was shown by Kon (1976*a*,*b*) that the formula for a derivative of the eigenvector can be written as

$$\frac{\partial E_{mv}^{(j)}}{\partial \theta} = \sum_{k \neq j} \frac{E_{mv}^{(k)} A_{kj}}{(\varepsilon_j - \varepsilon_k)} \tag{24}$$

where

$$A_{kj} = \sum_{mv} E_{mv}^{(k)} \frac{\partial (G')_{mm}^{vv}}{\partial \theta} E_{mv}^{(j)}. \tag{25}$$

Here, only non-degenerate solutions are assumed and we take into account the fact that only the diagonal elements of the matrix G' depend on θ. It directly follows from equation (24) that a small distance between the branches of the DS leads to an increase in the derivative of the eigenvector. The smallest distance occurs at the central point.

Considering various branches of the DS, it is possible to find a correspondence between the angle θ and the coordinate x at the section topograph. For each branch of the DS the integrand in equation (13) is an exponential function of the complex argument. According to the stationary phase approximation, the main contribution to the integral gives the region where the phase derivative equals zero.

On the line $\varphi = 0$ we have the next equation from this condition:

$$x_j(\theta) = z_t \theta - t E_{1j}(\theta), \quad E_{1j}(\theta) = \frac{1}{2K} \frac{\partial \varepsilon_j}{\partial \theta}. \tag{26}$$

We note that the inequalities $-X_t < tE_{1j} < 0$ follow from calculations and have a simple geometrical sense from multi-beam Takagi equations. The calculations show that if $z_t = 0$ then the central point $\theta = 0$ corresponds to $x_j = x_0 = -X_t/2$ for all branches of the DS. The point x_0 is the central point of the section topograph.

We are interested in the branches with the smallest absorption coefficient. For p polarization branch 8 has maximum excitation at $\theta_{m8} < 0$ and calculations show that $x_0 < x_{m8}$. Therefore, the bright maximum at the right of the section topograph corresponds to only this branch, and interference is impossible. For s polarization branch 7 has maximum excitation at $\theta_{m7} < 0$ and calculations show that $x_0 < x_{m7} < x_{m8}$. On the other hand, interference is more pronounced for s polarization at the central region of the topograph.

Finally, we can conclude that an analysis of the angular dependence of plane-wave six-beam diffraction and usage of the stationary phase method allow us to understand peculiarities of the section topographs of six-beam diffraction for a thick crystal. We can also estimate the role of distance z_t. For θ = 1 μrad and z_t = 100 cm the shift of coordinate Δx = 1 μm which is much less than X_t = 3.23 cm.

The effect of X-ray super-transmission can be used for a quality diagnostic of a thick silicon single crystal by means of comparison of the measured effective absorption coefficient with the results of calculation. It is of interest to study the interaction of a power radiation of an X-ray free-electron laser with a single crystal under the conditions of very little absorption.

We note that our method of computer simulations is valid for all multiple X-ray diffraction cases with three, four, five, six, eight, 12 strong waves or more. We will consider other cases in future work.

References

Afanas'ev, A. M. & Kohn, V. G. (1977). *Acta Cryst.* A**33**, 178–184.

Authier, A. (2005). *Dynamical Theory of X-ray Diffraction*, 3rd ed. Oxford University Press.

Chang, S.-L. (2004). *X-ray Multiple-Wave Diffraction: Theory and Application.* Springer Series in Solid-State Sciences. Berlin: Springer.

Giardina, M. D. & Merlini, A. (1973). *Z. Naturforsch. Teil A*, **28**, 1360.

Hildebrandt, G., Stephenson, J. D. & Wagenfeld, H. (1975). *Z. Naturforsch. Teil A*, **30**, 697–707.

Joko, T. & Fukuhara, A. (1967). *J. Phys. Soc. Jpn*, **22**, 597–604.

Kohn, V. G. & Khikhlukha, D. R. (2016). *Acta Cryst.* A**72**, 349–356.

Kohn, V. G. & Toneyan, A. H. (1986). *Acta Cryst.* A**42**, 441–449.

Kon, V. G. (1976*a*). *Fiz. Tverd. Tela (Leningr.)*, **18**, 2538–2545.

Kon, V. G. (1976*b*). *Sov. Phys. Solid State*, **18**, 1482–1486.

Miao, J., Ishikawa, T., Johnson, B., Anderson, E. H., Lai, B. & Hodgson, K. O. (2002). *Phys. Rev. Lett.* **89**, 088303.

Okitsu, K. (2003). *Acta Cryst.* A**59**, 235–244.

Okitsu, K., Imai, Y., Ueji, Y. & Yoda, Y. (2003). *Acta Cryst.* A**59**, 311–316.

Okitsu, K., Imai, Y. & Yoda, Y. (2012). *Recent Advances in Crystallography*, ch. 3, edited by J. B. Benedict. InTech, doi: 10.5772/47846.

Okitsu, K., Yoda, Y., Imai, Y., Ueji, Y., Urano, Y. & Zhang, X. (2006). *Acta Cryst.* A**62**, 237–247.

Sano, H., Ohtaka, K. & Ohtsuki, Y.-H. (1969). *J. Phys. Soc. Jpn*, **27**, 1254–1261.

Umeno, M. (1970). *Phys. Status Solidi A*, **2**, K203–K205.